Application of image-guided full waveform inversion to a 2D ocean-bottom cable data set

Yong Ma[1], Jianxin (Jerry) Yuan[2], Yunqing Shen[2] & Bin Gong[3]
[1] *Center for Wave Phenomena, Colorado School of Mines, Golden, CO 80401, USA*
[2] *Seismic Technology, ConocoPhillips Company, Houston, TX 77252, USA*
[3] *Formerly Seismic Technology, ConocoPhillips Company, Houston, TX 77252, USA; presently In-Depth Geophysical, Houston, TX 77074, USA*

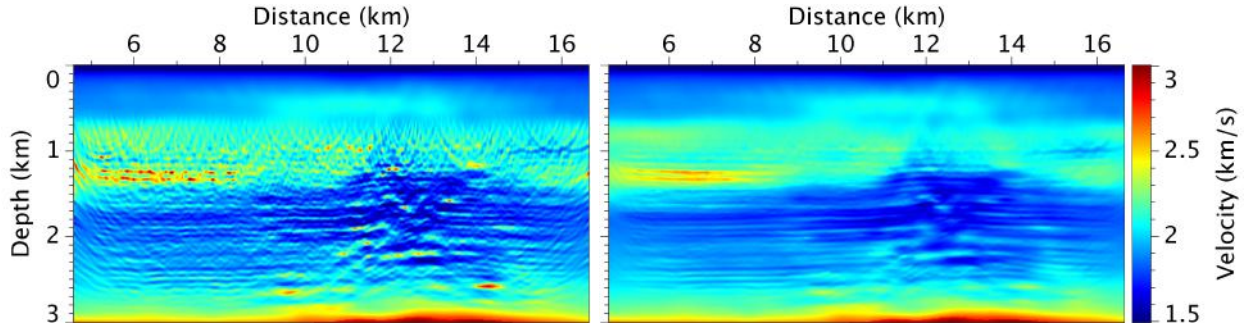

Figure 1. Estimated velocities with the conventional reflection FWI (a) and the image-guided reflection FWI (b).

ABSTRACT

Image-guided full waveform inversion (IGFWI) was proposed and synthetically tested in Ma et al. (2011). Compared with conventional FWI, IGFWI yields models (e.g., velocities) that make better geologic sense because it takes into consideration the subsurface structures, which can be apparent in migrated seismic images. Moreover, IGFWI converges faster in fewer iterations, especially when reflection energy is used to invert for high-wavenumber details in the model. We test IGFWI on a 2D ocean-bottom cable (OBC) data set. We first use refraction data to update the low-wavenumber component of the model and then proceed to invert for high-wavenumber details with reflection data. In the reflection stage, we incorporate structural constraints in the inversion; as a result, the estimated model makes plausible geologic sense.

Key words: full waveform inversion, image-guided, OBC data

1 INTRODUCTION

Full waveform inversion (FWI) (Tarantola, 1984) uses recorded seismic data $\mathbf{d}$ to estimate parameters of a subsurface model $\mathbf{m}$ by minimizing the difference between recorded data $\mathbf{d}$ and synthetic data $\mathbf{F}(\mathbf{m})$, where $\mathbf{F}$ is a forward operator that synthesizes data. In FWI, the objective function often takes an L2 norm: $E(\mathbf{m}) = \frac{1}{2}\|\mathbf{d} - \mathbf{F}(\mathbf{m})\|^2$.

A typical implementation of FWI based on conjugate gradients consists of three steps performed iteratively, beginning with an initial model $\mathbf{m}_0$:

(i) compute the gradient of the objective function $\mathbf{g}_i$ using the adjoint-state method (Tromp et al., 2005);
(ii) search for a step length α_i in the direction $\mathbf{h}_i(\mathbf{g}_i, \mathbf{g}_{i-1})$ (Vigh and Starr, 2008);
(iii) update the model with $\mathbf{m}_{i+1} = \mathbf{m}_i - \alpha_i \mathbf{h}_i$.

In each iteration, one needs to find a proper

step length that decreases the objective function. A quadratic line-search algorithm is performed to find this step length, and the search direction $\mathbf{h}_i$ is defined by the conjugate gradient as

$$\begin{aligned} \mathbf{h}_0 &= \mathbf{g}_0 \ , \\ \beta_i &= \frac{\mathbf{g}_i^T \left(\mathbf{g}_i - \mathbf{g}_{i-1}\right)}{\mathbf{g}_{i-1}^T \mathbf{g}_{i-1}} \ , \\ \mathbf{h}_i &= \mathbf{g}_i + \beta_i \mathbf{h}_{i-1} \ . \end{aligned} \tag{1}$$

FWI is a computationally intensive tool. It requires multiple iterations to minimize the data misfit; in each iteration, the cost of both the gradient calculation and the line search is equivalent to the cost of several seismic wavefield simulations and reconstructions, which are especially expensive in 3D.

In addition to its computational cost, FWI also suffers from nonuniqueness because FWI, as a typical inverse problem, is a underdetermined problem. In other words, many different models may yield synthetic data that match recorded data within a reasonable tolerance. This nonuniqueness is caused mainly by local minima in the data misfit function, and the presence of local minima is due to cycle skipping and the nonlinearity in the forward operation $\mathbf{F}(\mathbf{m})$. Strong nonlinearity in reflection FWI makes this local-minima problem more severe (Snieder et al., 1989). Cycle skipping occurs if the time delay between synthetic and recorded data is larger than half a period of the dominating wavelet. In practice, the cycle-skipping problem typically appears because it can be difficult to obtain an adequate initial model that is consistent with unrecorded low frequencies.

Both local-minima and cycle-skipping problems lead to models that poorly approximate the subsurface. To mitigate such problems, multiscale approaches (Bunks, 1995; Sirgue and Pratt, 2004; Boonyasiriwat et al., 2009) have been proposed. The fidelity of multiscale techniques depends fundamentally on the fidelity of low-frequency content in recorded data. In practice, the low frequencies required to bootstrap the multiscale approach may be unavailable.

Ma et al. (2011) propose image-guided FWI (IGFWI) to deal with these problems in a sparse model space, where conventional FWI is posed as a sparse inverse problem. The model $\mathbf{m}$ estimated in conventional FWI is densely sampled for simulating wave propagation. The number of dense samples is far beyond the number of necessary samples needed to geologically explain the model. To reduce the number of required iterations, one may use a sparse representation of the model and reduce the number of model parameters. In inversion, we then should choose as few samples as possible to construct a sparse model $\mathbf{s}$ while still maintaining as many geological features as possible. Between the dense model $\mathbf{m}$ and the sparse model $\mathbf{s}$, we define a linear relationship $\mathbf{m} = \mathbf{R}\mathbf{s}$, where $\mathbf{R}$ can take different forms. Various bases (e.g., Fourier bases, wavelet bases, and splines) have been used, typically in tomographic studies, to obtain different sparse models. Among these methods, the representative one is the wavelet transform (Meng and Scales, 1996; Loris et al., 2007; Simons et al., 2011). However, this type of model parameter reduction does not consider the subsurface structures, and as a result, it risks generating geologically non-plausible inversion results. In IGFWI, we implement $\mathbf{R}$ and $\mathbf{R}^T$ with the image-guided interpolation (IGI) (Hale, 2009) and its adjoint operator(Ma et al., 2010), respectively, in order to apply structural constraints derived from migrated images.

In the sparse model space $\mathbf{s}$, we represent FWI as a sparse inverse problem, in which we minimize a new objective function: $E(\mathbf{s}) = \frac{1}{2}\|\mathbf{d} - \mathbf{F}(\mathbf{R}\mathbf{s})\|^2$. The nonlinear conjugate-gradient method is still valid for us to solve for the sparse model $\mathbf{s}$ iteratively. The line search for this case is performed in a new update direction $\mathbf{h}_i^{\mathbf{s}}$, which is defined as (Ma et al., 2010)

$$\begin{aligned} \mathbf{h}_0^{\mathbf{s}} &= \mathbf{R}^T \mathbf{g}_0 \ , \\ \beta_i &= \frac{\left(\mathbf{R}^T \mathbf{g}_i\right)^T \left(\mathbf{R}^T \mathbf{g}_i - \mathbf{R}^T \mathbf{g}_{i-1}\right)}{\left(\mathbf{R}^T \mathbf{g}_{i-1}\right)^T \mathbf{R}^T \mathbf{g}_{i-1}} \ , \\ \mathbf{h}_i^{\mathbf{s}} &= \mathbf{R}^T \mathbf{g}_i + \beta_i \mathbf{h}_{i-1}^{\mathbf{s}} \ . \end{aligned} \tag{2}$$

In reality, we need a dense model $\mathbf{m}$ to compute synthetic data $\mathbf{F}(\mathbf{m})$ and to fit recorded data $\mathbf{d}$. For this reason, we apply the interpolation operator $\mathbf{R}$ to both sides of equation 2 in IGFWI and thereby interpolate the update direction $\mathbf{h}_i^{\mathbf{s}}$ in equation 2 to obtain an image-guided update direction $\mathbf{h}_i^{\mathbf{m}}$, which corresponds to the dense model space:

$$\begin{aligned} \mathbf{h}_0^{\mathbf{m}} &= \mathbf{R}\mathbf{R}^T \mathbf{g}_0 \ , \\ \beta_i &= \frac{\left(\mathbf{R}^T \mathbf{g}_i\right)^T \left(\mathbf{R}^T \mathbf{g}_i - \mathbf{R}^T \mathbf{g}_{i-1}\right)}{\left(\mathbf{R}^T \mathbf{g}_{i-1}\right)^T \mathbf{R}^T \mathbf{g}_{i-1}} \ , \\ \mathbf{h}_i^{\mathbf{m}} &= \mathbf{R}\mathbf{R}^T \mathbf{g}_i + \beta_i \mathbf{h}_{i-1}^{\mathbf{m}} \ . \end{aligned} \tag{3}$$

We then can use the image-guided conjugate-gradient method in equation 3 to update the dense model while maintaining the advantages of sparse inversion.

An implementation of IGFWI based on conjugate gradients consists of four steps performed iteratively, beginning with an initial model $\mathbf{m}_0$:

(i) compute the gradient $\mathbf{g}_i$, $\mathbf{R}^T\mathbf{g}_i$, $\mathbf{R}\mathbf{R}^T\mathbf{g}_i$;
(ii) search for a step length α_i in the direction $\mathbf{h}_i^{\mathbf{m}}$;
(iii) update the model with $\mathbf{m}_{i+1} = \mathbf{m}_i - \alpha_i \mathbf{h}_i^{\mathbf{m}}$;
(iv) remigrate with the updated model and reselect the sparse model based on the remigrated image.

Although the four-step procedure finally gives a dense model solution, it in fact maintains the advantages of sparse inversion. In the sparse inversion, each parameter in the sparse model space $\mathbf{s}$ represents an area in the dense model space $\mathbf{m}$. This sparse representation causes more blocky updates in the model and the blockiness can mitigate the absence of low frequencies in field data. Because the structural features of the subsurface

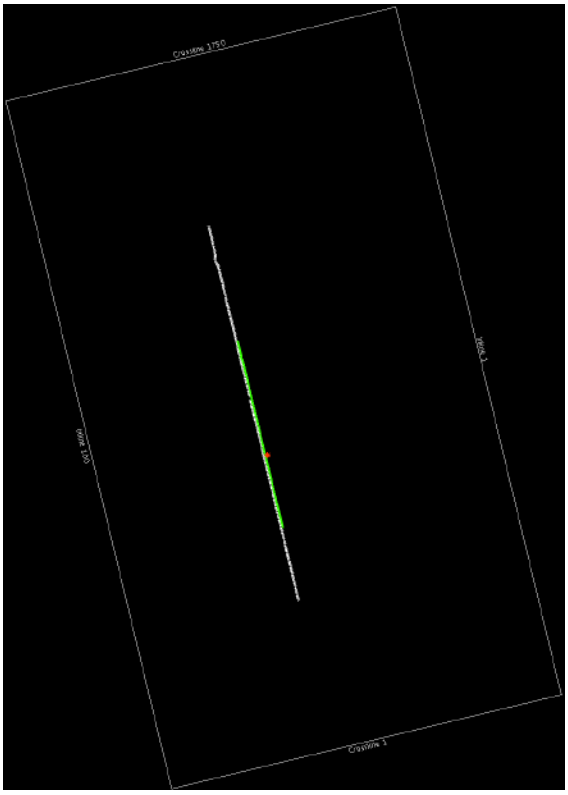

Figure 2. One 2D survey line extracted from a 3D OBC survey. The red dot indicates the location of a shot; white dots are receivers spanning about 12 km; green dots are common-depth point locations.

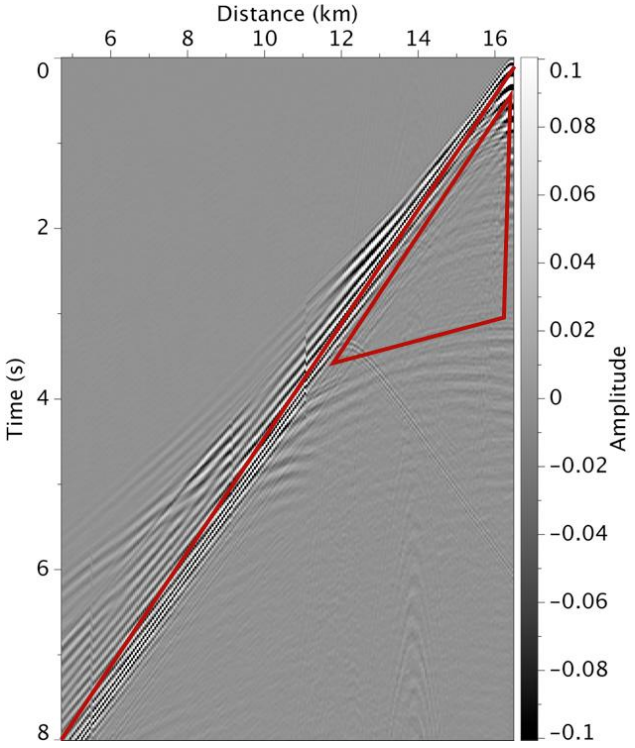

Figure 3. One typical shot gather for the 2D OBC data set. This shot gather shows an offset of about 12 km. Because of this large offset, significant refraction energy appears at far offset. The red line indicates the traveltime of the direct arrival and energy that arrives earlier than this line is refraction.

are taken into consideration as constraints in the sparse inversion, IGFWI generates models that make better geological sense than conventional FWI does. Ma et al. (2011) test IGFWI in the synthetic Marmousi model. In this paper, we test IGFWI on a real 2D OBC data set.

2 DATA

2.1 Field data

Figure 2 shows the source and receiver lines of this 2D data set in a survey map. The entire 2D data set consists of 24 shots and 235 receivers. Shot and receiver spacings are about 500 m and 50 m, respectively. Sources are 5 m below the water surface; receivers are on the sea floor (70 m beneath the water surface). In this OBC survey, both primary and converted waves are collected; however, we only use the P-wave component of the data set in inversion.

Figure 3 shows one P-wave shot gather for the 2D data set; the largest offset is about 12 km. Due to the large offset of the survey, this data set contains significant refraction energy, especially in the far offset. As illustrated in Figure 3, the red line indicates the traveltime of the direct wave; refraction energy arrives earlier than the direct wave. Because of the shallow water depth (70 m), strong surface-related multiples are present in the original data set. However, no processing is done to remove these surface-related multiples. The original data set has a very wide frequency band. A bandpass filter is applied to the original data set to obtain the data between 4 Hz and 20 Hz, shown in Figure 3.

2.2 Source wavelet

Estimation of a source wavelet is an essential step in FWI. In this field data test, the source wavelet for inversion is obtained from a source signature measured in the laboratory. Figure 4a shows the source signature after de-bubbling; its spectrum (Figure 4b) has a much wider range than the effective frequency band (4 – 20 Hz) of the data set. We apply a minimum phase bandpass filter to the source signature and obtain a source wavelet (Figure 5a), with a spectrum (Figure 5b) that matches the frequency band of the data set.

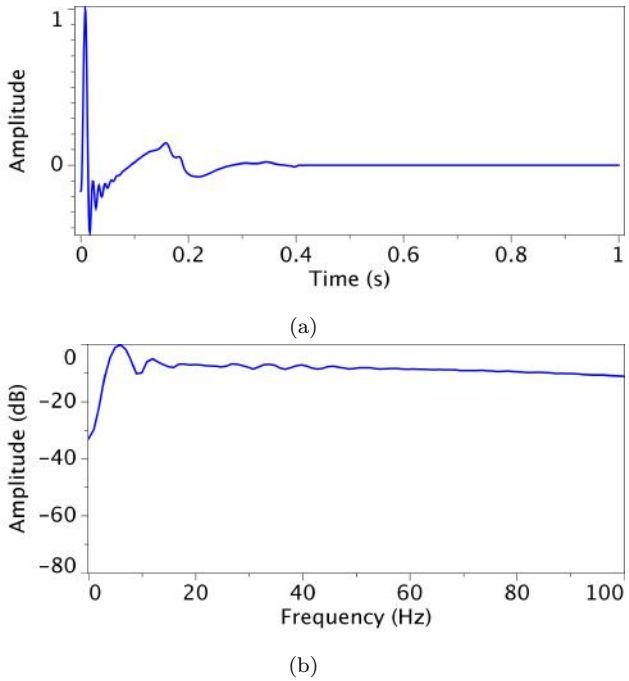

Figure 4. Source signature (a) that is measured in laboratory and its spectrum (b).

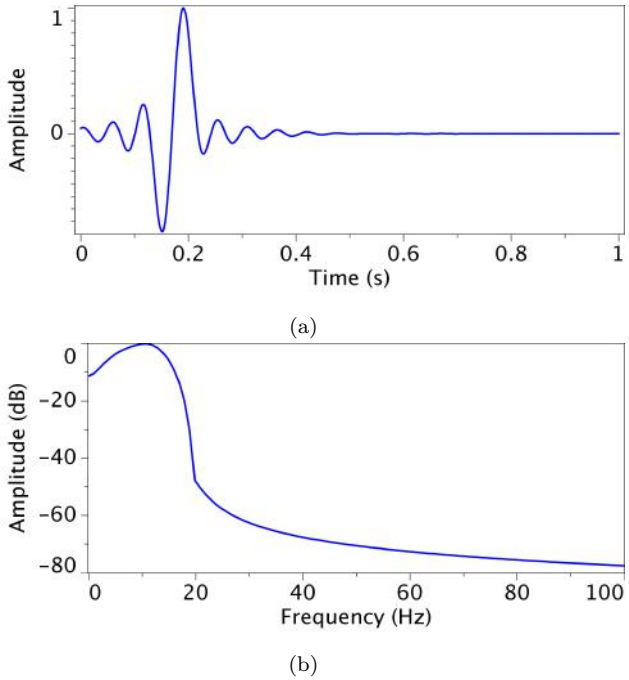

Figure 5. Source wavelet (a) that is used for inversion and its spectrum (b). This source wavelet is obtained by applying a bandpass filter to the source signature in Figure 4a.

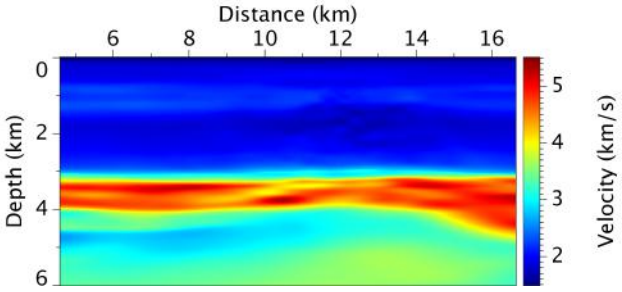

Figure 6. Initial velocity model.

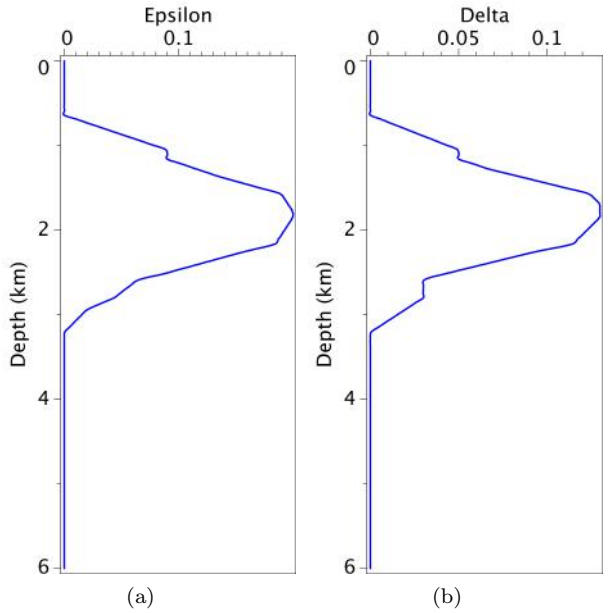

Figure 7. 1D profiles of anisotropy parameters: ϵ (a) and δ (b).

3 METHODOLOGY

3.1 Synthetic data

The survey area is known to have strong vertical transparent isotropy (VTI). Figure 6 shows the initial P-wave velocity model that is produced by traveltime tomography and used in full waveform inversion. Figure 7a and 7b show 1D profiles of the Thomsen parameters ϵ and δ, respectively. These anisotropic parameters are not exact because they are borrowed from another field that is nearby.

To honor the strong VTI effect in wave propagation, we solve an acoustic VTI wave equation (Chu et al., 2011) that uses the pseudo-acoustic approximation (Alkhalifah, 2000) to simulate the synthetic data. One example of the 2D acoustic VTI wave equation contains two coupled partial differential equations (Du

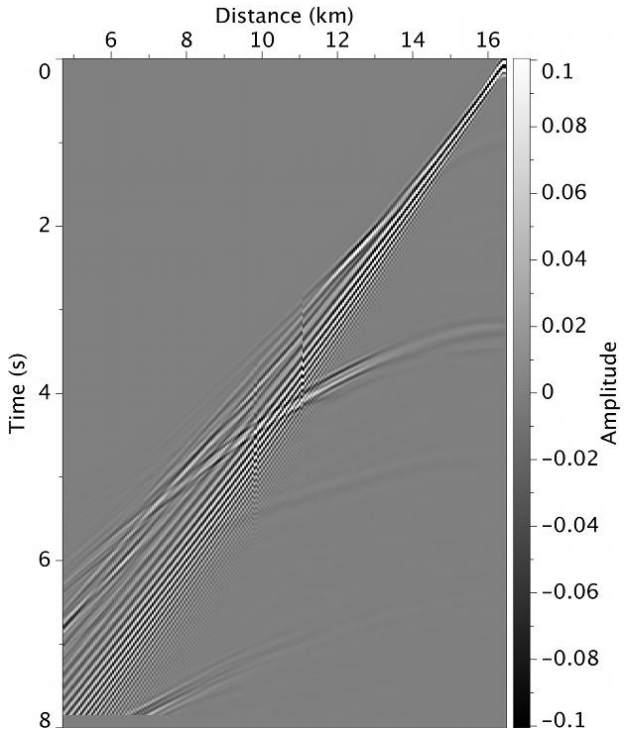

Figure 8. Synthetic data simulated with the initial velocity model and anisotropic parameters.

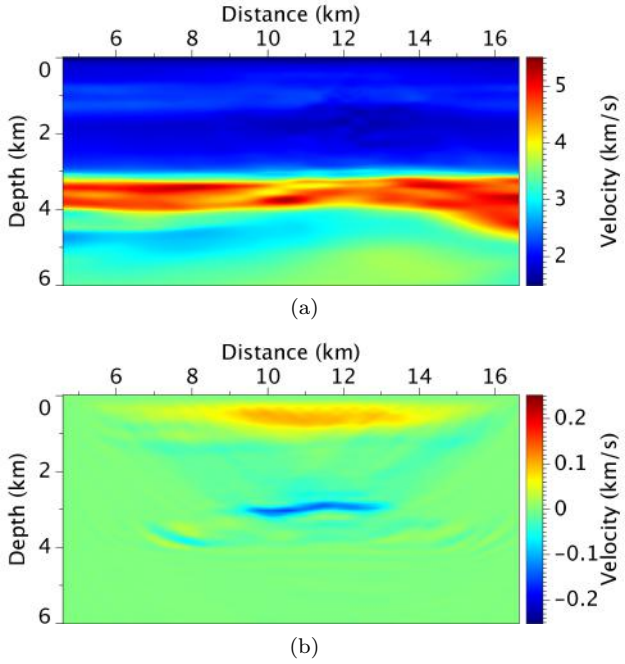

Figure 9. Estimated velocity (a) after 5 iterations of refraction FWI and the difference (b) between this estimation and the initial velocity.

et al., 2008):

$$\frac{\partial^2 \mathbf{p}}{\partial t^2} = \mathbf{v}_{px}^2 \frac{\partial^2 \mathbf{p}}{\partial x^2} + \mathbf{v}_{pz}^2 \frac{\partial^2 \mathbf{q}}{\partial z^2} \tag{4}$$

and

$$\frac{\partial^2 \mathbf{q}}{\partial t^2} = \mathbf{v}_{pn}^2 \frac{\partial^2 \mathbf{p}}{\partial x^2} + \mathbf{v}_{pz}^2 \frac{\partial^2 \mathbf{q}}{\partial z^2} \ , \tag{5}$$

where $\mathbf{p}$ and $\mathbf{q}$ are P- and S-waves, respectively; $\mathbf{v}_{pz}$ (Figure 6) is the P-wave velocity along the symmetry axis; $\mathbf{v}_{px} = \mathbf{v}_{pz}\sqrt{1+2\epsilon}$, and $\mathbf{v}_{pn} = \mathbf{v}_{pz}\sqrt{1+2\delta}$.

In this study, we only care about the P-wave. Figure 8 shows the synthetic P-wave data simulated with the initial velocity and the Thomsen parameters. If we ignore the VTI anisotropy by using an isotropic acoustic wave equation, the synthetic data has more significant traveltime error in the far offset.

3.2 Refraction FWI + reflection FWI

Because significant refraction energy is available in the far offset, we can first use the refraction energy to update the velocity model. In this stage of FWI, we only match seismograms that arrive earlier than the direct wave, indicated by the red line in Figure 3. After updating low-wavenumber components of the velocity with refractions, we then use the reflection information in the data set to update high-wavenumber details of the model. The reflection data that we use for inversion is within the red triangle region, where the maximum zero-offset time is approximately 3 s.

Conventional FWI is performed to implement the inversion with refraction data. When proceeding to the inversion with reflection data, we use IGFWI and compare IGFWI results with conventional FWI results. Both conventional FWI and IGFWI are implemented with a time-domain approach, which is equivalent to inverting the entire frequency band (4 – 20 Hz) simultaneously in the frequency domain.

4 INVERSION RESULTS

4.1 Inversion with refraction data

Figure 9a displays the estimated velocity model after 5 iterations of FWI with refraction data. Because FWI uses only the refraction energy, it only updates the velocity model with low-wavenumber components, which is indicated by the accumulated velocity update (Figure 9b) in these 5 iterations.

4.2 Inversion with reflection data

In order to allow FWI to update the velocity model with high-wavenumber details, we need to use reflection data. In this stage of reflection FWI, we employ the refraction-FWI-updated velocity model (Figure 9a) as

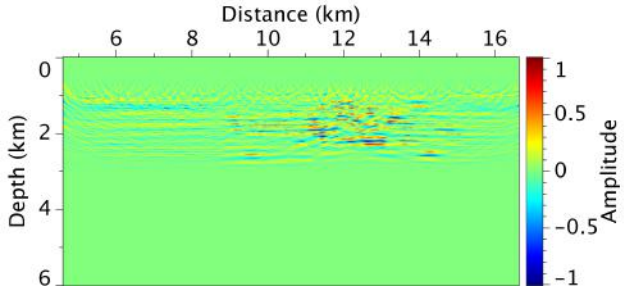

Figure 10. Gradient **g** of the objective function in reflection FWI. The velocity for computing this gradient is the refraction-FWI updated model in Figure 9a.

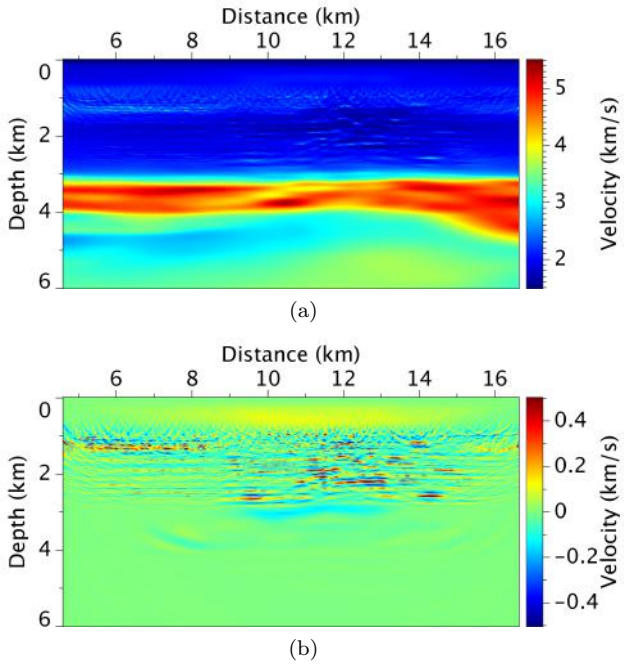

Figure 11. Estimated velocity (a) after 5 iterations of reflection FWI and the difference (b) between this estimation and the initial velocity.

the initial velocity model. Both conventional FWI and IGFWI are tested using the reflection data.

4.2.1 Conventional FWI

We first compute the gradient of the objective function using the adjoint-state method. In other words, the gradient is achieved by performing a reverse-time migration (RTM) of the data residual $\mathbf{d} - \mathbf{F}(\mathbf{m}_i)$ with the current velocity model $\mathbf{m}_i$. Figure 10 shows an example of the gradient of the objective function in the reflection FWI. This gradient is computed with the velocity (Figure 9a) that is estimated by conventional FWI with the refraction data. We then use a quadratic line search method to

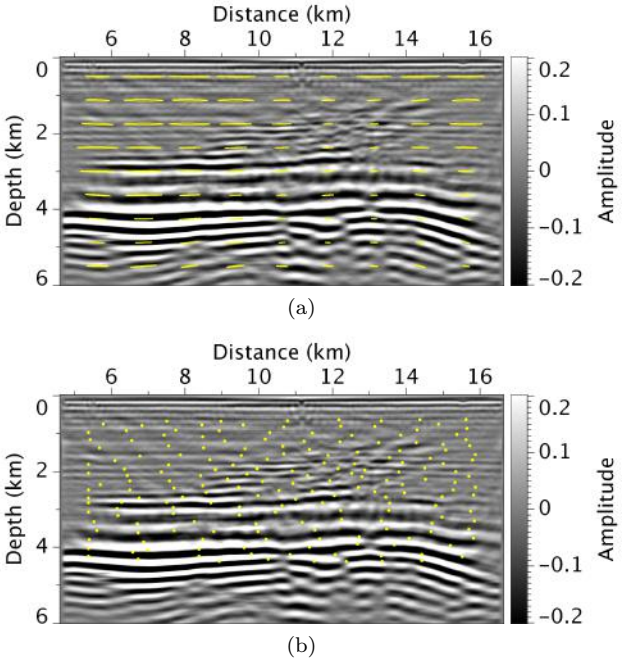

Figure 12. Structure features (a) indicated by tensor fields (ellipses) and a sparse model represented by dots (b).

update the velocity model. Figure 11a shows the velocity updated by conventional FWI, which employs the reflection data in 5 iterations. The difference between the reflection-FWI-updated velocity and the initial velocity is shown in Figure 11b. Unlike the refraction inversion (Figure 9b), the inversion with reflection data updates the velocity model with more details by generating high-wavenumber components, as illustrated in Figure 11b. However, the high-wavenumber details are contaminated by many artifacts that are not geologically sensible.

4.2.2 Image-guided FWI

The IGFWI procedure is similar as that of conventional FWI because the nonlinear conjugate-gradient method and the quadratic line search algorithm are the same. The difference is that, instead of computing the gradient $\mathbf{g}_i$, IGFWI computes the projected gradient $\mathbf{R}^T\mathbf{g}_i$ and the image-guided gradient $\mathbf{R}\mathbf{R}^T\mathbf{g}_i$. In order to do this, we must first know the structural information of the subsurface and then construct a sparse model according to the structural features.

Figure 12a displays an RTM image of the 2D OBC data, which is migrated with the initial velocity model. On top of the migrated image, ellipses illustrate the structural features of the subsurface, e.g., coherence, orientation. For this field data example, the subsurface structure is horizontally coherent in most areas. Figure 12b shows a sparse model space that is constructed

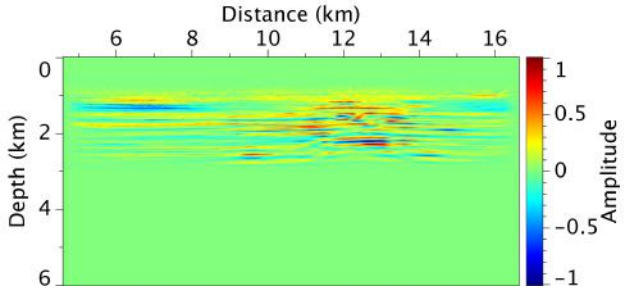

Figure 13. Image-guided gradient $\mathbf{RR}^T\mathbf{g}$ of the objective function in reflection FWI. The velocity for computing this gradient is the refraction-FWI updated model in Figure 9a.

with the structure-constrained selection scheme (Ma et al., 2011).

Using the structural constraints and the sparse model, we compute the image-guided gradient $\mathbf{RR}^T\mathbf{g}_i$, shown in Figure 13. This image-guided gradient is achieved in two steps. We first apply the adjoint image-guided interpolation operator $\mathbf{R}^T$ to the gradient $\mathbf{g}_i$ and obtain the projected gradient $\mathbf{R}^T\mathbf{g}_i$. This step projects (*gathers*) the gradient information to the chosen sparse model space. We then apply the image-guided interpolation operator $\mathbf{R}$ to the projected gradient $\mathbf{R}^T\mathbf{g}_i$ and get the image-guided gradient $\mathbf{RR}^T\mathbf{g}_i$. This step interpolates (*scatters*) the projected gradient from the sparse to the dense model space. Compared to the regular gradient (Figure 10), the image-guided gradient (Figure 13) contains fewer artifacts and better honors the structural features. Moreover, the gather-scatter process produces low wavenumber components in the image-guided gradient.

The nonlinear conjugate-gradient method (equation 3) takes the projected gradient $\mathbf{R}^T\mathbf{g}_i$ and the image-guided gradient $\mathbf{RR}^T\mathbf{g}_i$ to compute the update direction $\mathbf{h}_i^{\mathbf{m}}$, employed in the subsequent quadratic line search. Figure 14a shows the velocity updated by the image-guided FWI, which uses the reflection data in 5 iterations. The difference between the reflection-IGFWI-updated velocity and the initial velocity is shown in Figure 14b.

4.3 Discussion

Because of limited data is used in inversion, velocity update mainly occurs in the area above 3 km. Figure 15 compares the initial velocity, refraction-FWI velocity, conventional reflection-FWI velocity, and the image-guided reflection-FWI velocity. The velocity in Figure 15d, which is obtained after image-guided reflection FWI, shows significantly improvement by removing geologically non-interpretable artifacts from the conventional reflection-FWI model (Figure 15c). Meanwhile, image-guided reflection FWI maintains the high-wavenumber details.

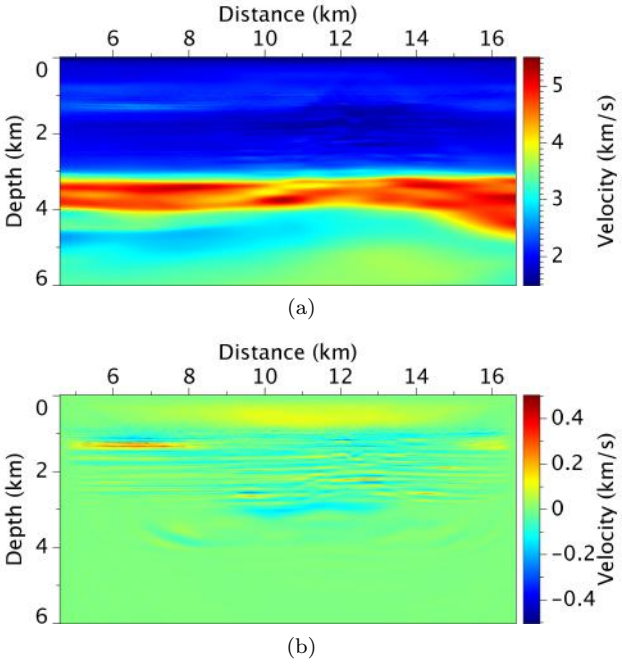

Figure 14. Estimated velocity (a) after 5 iterations of image-guided reflection FWI and the difference (b) between this estimation and the initial velocity.

In this field data test, the synthetic data takes into account of VTI anisotropy, but the anisotropic parameters may not be exact because they are estimated for another nearby field. Therefore, the estimated velocity model may have errors to trade off the ambiguity between the velocity itself and the anisotropy parameters.

RTM is used to test the inversion results. Figure 16 displays the RTM images of the 2D OBC data set, which is migrated with the initial velocity, refraction-FWI velocity, conventional reflection-FWI velocity, and image-guided reflection-FWI velocity, respectively. In the circle-highlighted area of Figure 16 have gas clouds been discovered. Despite the existence of gas clouds, rock layers should maintain the structural continuity. However, broken structures are observed in the highlighted area of Figures 16a and16b. In contrast, Figures 16c and16d show more interpretable coherent structures, especially in the highlighted gas cloud area. Moreover, the migrated image in Figure 16d, which is done with the image-guided reflection-FWI velocity, contains less artifacts than Figure 16c.

Each iteration of the IGFWI is more expensive than one iteration of conventional FWI as steps (i) and (iv) bring additional cost. Fortunately, the cost of applying the interpolation and its adjoint operator or reselecting a sparse model is negligible compared to the cost of forward modeling or reverse time migration. Also, it is not necessary to reselect the sparse model in every iteration,

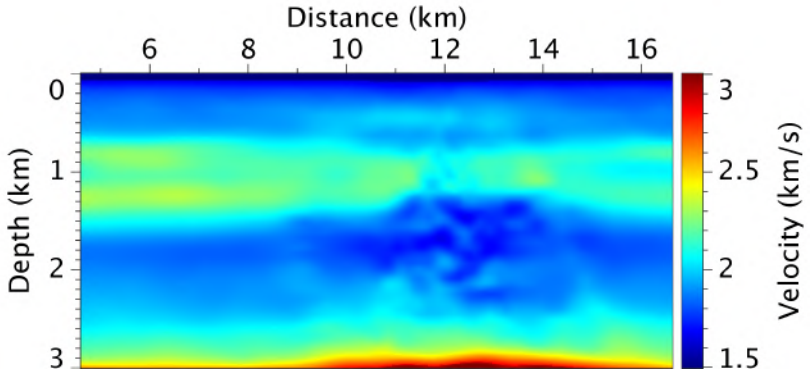

(a)

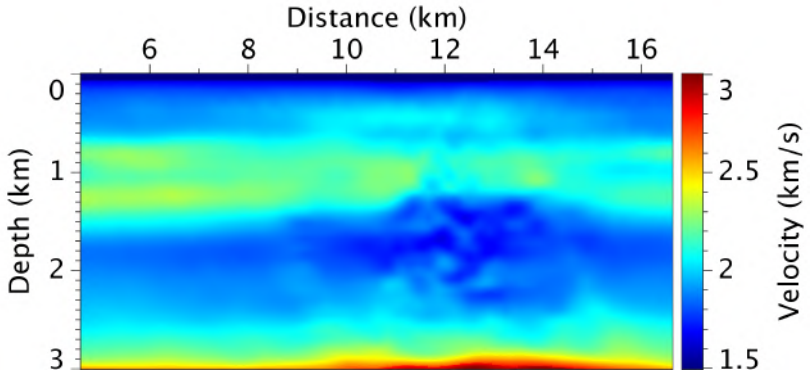

(b)

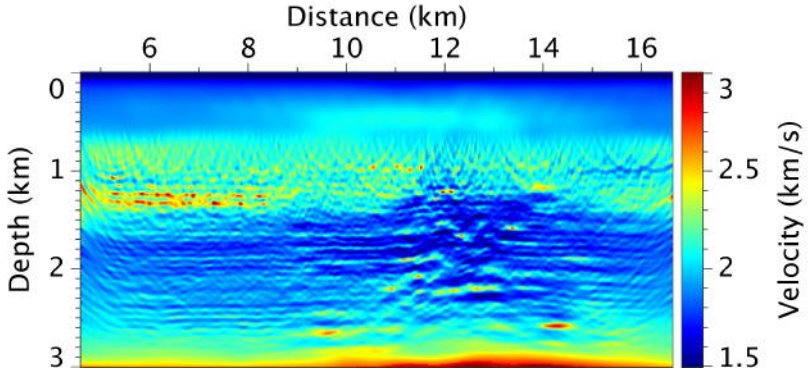

(c)

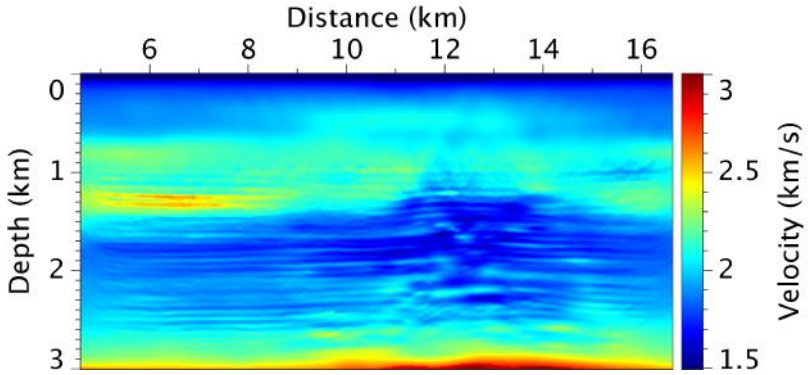

(d)

Figure 15. Zoom-in views of initial model (a), refraction updated model (b), reflection updated model (c), and image-guided reflection updated model (d).

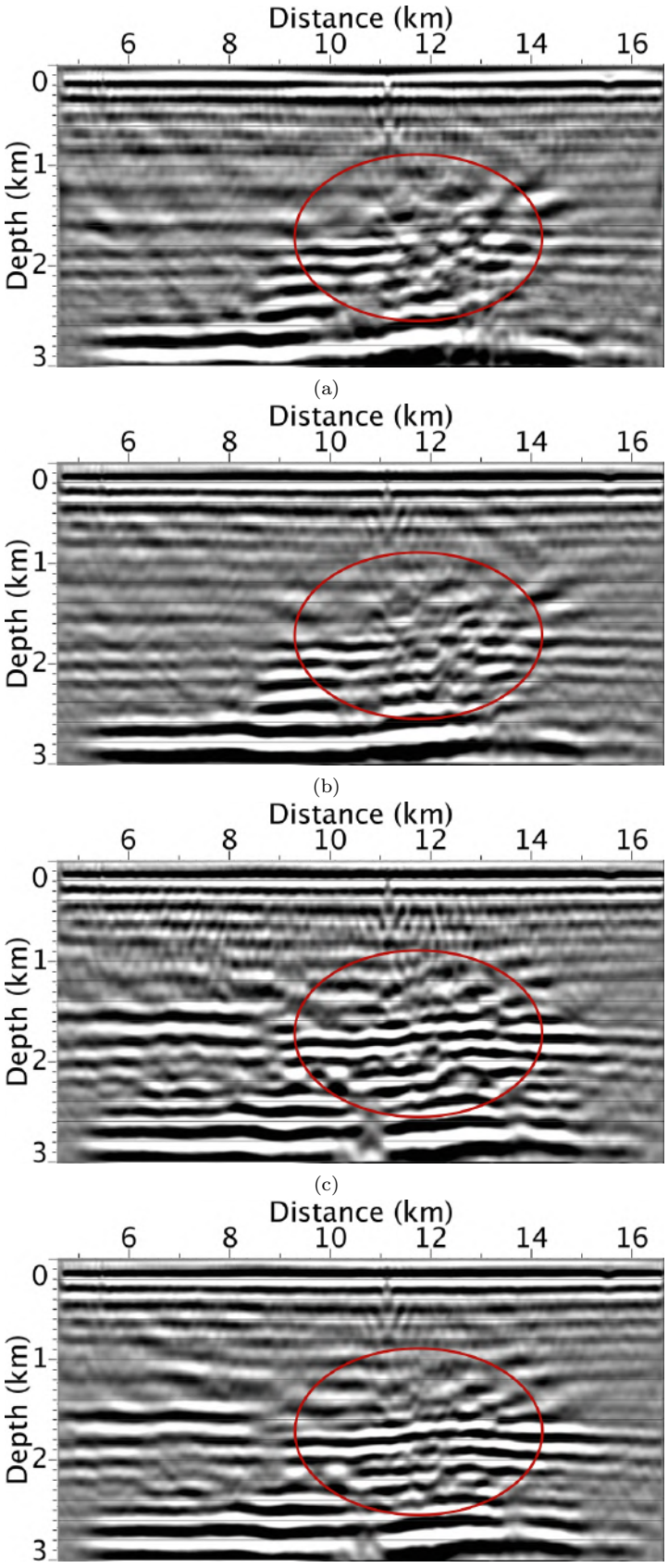

Figure 16. RTM with initial model (a), refraction-FWI model (b), reflection-FWI model (c), and image-guided reflection-FWI model (d).

and therefore by applying the last step only in selected iterations, we can further reduce the cost.

5 CONCLUSION

We have demonstrated the capability of IGFWI for estimating velocity models with a 2D OBC data set. The refraction and reflection data are sequentially used to update the velocity model. Compared to conventional reflection FWI, IGFWI with reflection data, which essentially solves a sparse inverse problem, generates velocity models that make better geological sense. This improvement is due to the fact that IGFWI uses the subsurface structures, which are extracted from the migrated seismic image, to constrain the inversion in the sparse model space. We compared RTM images of the 2D OBC data using velocity models that are updated by conventional FWI and IGFWI. With the IGFWI-estimated velocity, RTM images show more interpretable coherent structures in the complex area, known to contain low-velocity gas clouds.

6 ACKNOWLEDGMENTS

Authors thank ConocoPhillips for the permission to publish this work, which was finished during Yong Ma's internship with the Seismic Technology group at ConocoPhillips in summer 2011. Yong wants to thank Yanqing Zeng for his generous help to make RTM images in this report. Yong is grateful to Chunlei Chu and Yi Wang for the reference to the acoustic VTI modeling that is employed in this study. Yong also wants to thank Kirk Wallace for his help to generate common-image gathers, which are used intermediately to QC the inversion.

REFERENCES

Alkhalifah, T., 2000, An acoustic wave equation for anisotropic media: Geophysics, **65**, 1239–1250.

Boonyasiriwat, C., P. Valasek, P. Routh, W. Cao, G. T. Schuster, and B. Macy, 2009, An efficient multiscale method for time-domain waveform tomography: Geophysics, **74**, WCC59–WCC68.

Bunks, C., 1995, Multiscale seismic waveform inversion: Geophysics, **60**, 1457.

Chu, C., B. K. Macy, and P. D. Anno, 2011, Accurate and efficient pure acoustic wave propagation in VTI media: 73rd EAGE Conference & Exhibition, Extended Abstracts.

Du, X., R. P. Fletcher, and P. J. Fowler, 2008, A new pseudo-acoustic wave propagation for VTI media: 70th EAGE Conference & Exhibition, Extended Abstracts.

Hale, D., 2009, Image-guided blended neighbor interpolation of scattered data: SEG Technical Program Expanded Abstracts, **28**, 1127–1131.

Loris, I., G. Nolet, I. Daubechies, and F. A. Dahlen, 2007, Tomographic inversion using L1-norm regularization of wavelet coefficients: Geophysical Journal International, **170**, 359–370.

Ma, Y., D. Hale, B. Gong, and Z. Meng, 2011, Image-guided full waveform inversion: CWP Report, **678**.

Ma, Y., D. Hale, Z. Meng, and B. Gong, 2010, Full waveform inversion with image-guided gradient: SEG Technical Program Expanded Abstracts, **29**, 1003–1007.

Meng, Z., and J. A. Scales, 1996, 2D tomography in multi-resolution analysis model space: SEG Technical Program Expanded Abstracts, **15**, 1126–1129.

Simons, F. J., I. Loris, G. Nolet, I. C. Daubechies, S. Voronin, J. S. Judd, P. A. Vetter, J. Charléty, and C. Vonesch, 2011, Solving or resolving global tomographic models with spherical wavelets, and the scale and sparsity of seismic heterogeneity: Geophysical Journal International, **187**, 969–988.

Sirgue, L., and R. G. Pratt, 2004, Efficient waveform inversion and imaging: A strategy for selecting temporal frequencies: Geophysics, **69**, 231.

Snieder, R., M. Y. Xie, A. Pica, and A. Tarantola, 1989, Retrieving both the impedance contrast and background velocity: A global strategy for the seismic reflection problem: Geophysics, **54**, 991–1000.

Tarantola, A., 1984, Inversion of seismic-reflection data in the acoustic approximation: Geophysics, **49**, 1259–1266.

Tromp, J., C. Tape, and Q. Liu, 2005, Seismic tomography, adjoint methods, time reversal and banana-doughnut kernels: Geophysical Journal International, **160**, 195–216.

Vigh, D., and E. Starr, 2008, 3D prestack plane-wave, full-waveform inversion: Geophysics, **73**, VE135–VE144.